Noise Reduction for Low-dose Single-slice Helical CT Sinogram

Jing Wang, Tianfang Li, Hongbing Lu, and Zhengrong Liang

Abstract—**Helical computed tomography (HCT) offers several advantages on conventional step-and-shoot CT for imaging a relatively large object, especially in dynamic studies. However, it may increase the x-ray exposure significantly. This work aims to reduce the radiation by noise reduction on low-dose (or mA) sinogram of HCT. The noise reduction method is based on three observations on HCT: (1) the axial sampling of HCT projections is nearly continuous as the detector system rotates; (2) the noise distribution in the sinogram space is nearly a Gaussian after system calibration (including logarithmic transform); and (3) the relationship of calibrated data mean and variance can be expressed as an exponential functional across the field-of-view. Based on the second and third observations, a penalized weighted least-square (PWLS) solution was chosen, where the weight is given by the data mean-variance relationship. The first observation encourages the use of Karhunen-Loève (KL) strategy along the axial direction. In the KL domain, the eigenvalue of each principal component was used for an adaptive noise smoothing via the penalty. The KL-PWLS noise-reduction method was implemented analytically for efficient reconstruction of large volume HCT images. Simulation studies demonstrated noticeable improvement, in terms of image quality measures and abnormal detectability observer studies, of the proposed noise-reduction method over conventional low-pass noise filtering with an optimal cutoff frequency and/or other filter parameters.**

I. Introduction

HELICAL/SPIRAL computed tomography (HCT) makes it possible to scan completely a vital organ volume in a single breath-hold, thus registration problem related to patient motion can be eliminated. In recent years, HCT has replaced conventional step-and-shoot CT in many clinical applications. Helical scanning is of significant benefit for CT angiography and multi-phase abdominal imaging. Although HCT has many advantages, the effective dose of HCT can be up to four times higher than that of a conventional step-and-shoot CT according to a recent report [1]. Minimizing x-ray exposure to the patients has been one of the major efforts in the CT field.

Manuscript received by October 20, 2004. This work was supported in part by the NIH National Heart, Lung and Blood Institute under Grant # HL54116 and the NIH National Cancer Institute under Grant # CA82402.

J. Wang is with the Departments of Radiology and Physics and Astronomy, State University of New York, Stony Brook NY 11794 USA (telephone: 631-444-2736, e-mail: jingwang @mil.sunysb.edu).

T. Li and Z. Liang are with the Department of Radiology, State University of New York, Stony Brook, NY 11794 USA.

H. Lu is with Department of Biomedical Engineering, the Fourth Military Medical College, Xi'An, Shangxi 710032 China.

A simple and cost-effective means among many strategies to achieve low-dose CT applications is to lower down x-ray tube current (mA) value (for both helical and stop-shoot modes). However, the image quality of low mA acquisition protocol will be severely degraded due to the excessive x-ray quantum noise. In addition, it has been shown [2] that helical weighting scheme in CT image reconstruction can result in non-uniform noise in the reconstructed images and increase noise level by 10%-40% relative to those images reconstructed by the conventional step-and-shoot CT. A high and non-uniform image noise will affect low-contrast detectability and other clinical assessment.

In this report, we present a Karhunen-Loève (KL) domain penalized-weighted least-square (PWLS) filtering scheme to reduce the noise of helical projections or sinogram after system calibration (including logarithmic transform). The statistical PWLS solution was calculated analytically to achieve the maximum reconstruction speed [3]. Simulation results showed that the noise in the reconstructed images is relatively uniform and low after the KL-PWLS filtering. It was also shown that small structures along the *z*-axis are well preserved. These favorable properties of KL-PWLS filtering could improve the detectbility in low-contrast environment. Receiver operating characteristic (ROC) study and Hotelling trace (HT) calculation quantitatively confirm this expectation.

II. Methods

Our previous analyses [4-6] strongly indicate that the calibrated projection data of low-dose CT follow approximately a Gaussian distribution with an associated relationship between the data mean and variance, which can be described by the following analytical formula:

$$\sigma_i^2 = f_i \times \exp(\lambda_i / S) \qquad (1)$$

where λ_i is the mean and σ_i^2 is the variance of the projection data at detector channel or bin i, S is a scaling parameter and f_i is a parameter adaptive to different detector bins. Based on the above noise properties of low-dose CT projection data, the PWLS solution is a statistically optimal choice. Considering the nearly continuous axial sampling in spiral mode, the potential of KL transform for processing of correlative information can be realized. The KL transform manipulates a sequence of correlated measurements into an

uncorrelated, ordered principle component series and, therefore, provides a unique means for noise reduction, feature extraction and de-correlation. This unique feature has been proved useful in tomographic image reconstruction [7].

Therefore, we proposed a KL domain PWLS smoothing scheme to reduce the low-dose HCT noise in the sinogram. In the proposed KL-PWLS approach, we chose neighboring 2π rotation projection datasets to perform the KL transform which accounts for the most correlative information among nearby measurements without noticeable increase of computing time. For example, for a specific 2π rotation projection dataset, one 2π rotation projection dataset before and the other 2π rotation projection dataset after the specific 2π rotation dataset were chosen to perform the KL transform. By this implementation, the element *kl* of the covariance matrix K_t of the calibrated projection data can be calculated as [7]:

$$[K_t]_{kl} = \frac{1}{N-1}\sum_{i=1}^{N}(y_{i,k} - \bar{y}_k)(y_{i,l} - \bar{y}_l) \qquad (2)$$

where $y_{i,k}$ is the *i*-th projection datum within *k*-th 2π rotation,

$$\bar{y}_k = \frac{1}{N}\sum_{i=1}^{N} y_{i,k} \qquad (3)$$

and *N* is the number of detector bins multiplied by the number of views within a 2π rotation. From the covariance matrix, the KL transform matrix *A* can be calculated, based on:

$$K_t A^T = A^T D\,. \qquad (4)$$

In equation (4) $D=diag\{d_l\}_{l=1}^{3}$, where d_l is the *l*-th eigenvalue of K_t. The dimension of K_t was chosen as 3 by 3 for the most nearby information, and the eigenvector in equation (4) can then be very efficiently computed. Thus, the KL transform for the selected neighboring 2π rotation projection datasets can be expressed as:

$$\tilde{y} = Ay\quad. \qquad (5)$$

For each KL component, the PWLS criterion was used to estimate the corresponding ideal projection. In general, the PWLS smoothing criterion in the KL domain estimates the ideal projection by minimizing the following objective function:

$$\Phi_l(\tilde{y}_l) = \tfrac{1}{2}(\tilde{y}_l - \tilde{\lambda}_l)^T \tilde{\Sigma}_l^{-1}(\tilde{y}_l - \tilde{\lambda}_l) + \tfrac{1}{2}\left(\frac{\alpha}{d_l}\right)\tilde{\lambda}_l^T M\ \tilde{\lambda}_l \qquad (6)$$

where $\tilde{y}_l$, and $\tilde{\lambda}_l$ are the *l*-th components of the KL transformed noisy projection and ideal projection, respectively. Notation *T* is the transpose operator and *M* is the matrix that reflects the relationship between neighborhood of data mean λ. Notation d_l is the eigenvalue associated with the *l*-th KL vector and $\tilde{\Sigma}$ is the diagonal variance matrix of $\tilde{y}_l$. The inverse variance matrix $\tilde{\Sigma}_l^{-1}$ can be estimated by [7]:

$$\tilde{\Sigma}_l^{-1} = diag\ \{\varphi_l^T Q_i^{-1}\varphi_l\}_{i=1}^{N} \qquad (7)$$

where $Q_i = diag\ \{\sigma_{i,k}^2\}_{k=1}^{3}$ is the variance matrix of the projection at bin *i* and φ_l is the *l*-th KL basis vector. For a given pixel in the projection image, a 3×3 window was used to estimate the sample mean, then the estimated sample mean was employed by equation (1) to calculate the sample variance $\sigma_{i,k}^2$ for the weight $\tilde{\Sigma}_l^{-1}$ of a weighted least square estimation. The penalty weighting parameter α for the PWLS estimation becomes the ratio α / d_l in the KL domain [7], as expected. Its dependence on the eignvalue is favorable because the regularization parameter varies adaptively according to the signal-to-noise (SNR) ratio of each component. A smaller KL eigenvalue is usually associated with a component having a lower SNR and, therefore, a larger regularization value should be used to penalize this noisier data. After the KL-PWLS estimated data were inverse KL transformed, the well-established filtered back-projection (FBP) method were used for slice reconstruction after interpolation to full scan [8].

TABLE I
PARAMETER OF THE MODIFIED 3D SHEPP-LOGAN PHANTOM *

Coordinates of center	Axis lengths	Rotation angles	Intensity
(0.0, 0.0, 0.0)	(0.69, 0.92, 0.9)	(0, 0)	1200
(0.0, -0.0184, 0.0)	(0.6624, 0.874, 0.88)	(0, 0)	-480
(-0.22, 0.0, -0.25)	(0.41, 0.16, 0.21)	(-72, 0)	-120
(0.22, 0.0, -0.25)	(0.31, 0.11, 0.22)	(72, 0)	-120
(0.0, 0.35, -0.25)	(0.21, 0.25, 0.35)	(0, 0)	60
(0.0, 0.10, -0.25)	(0.046, 0.046, 0.046)	(0, 0)	60
(0.0, -0.10, -0.25)	(0.046, 0.046, 0.046)	(0, 0)	60
(-0.08, -0.605, -0.25)	(0.046, 0.023, 0.02)	(0, 0)	60
(0.06, -0.605, -0.25)	(0.046, 0.023, 0.02)	(90, 0)	60
(0.0, -0.605, -0.25)	(0.023, 0.023, 0.023)	(0, 0)	60
(0.0, -0.105, 0.625)	(0.056, 0.04, 0.10)	(90, 0)	120
(0.0, 0.10, 0.625)	(0.056, 0.056, 0.10)	(0, 0)	-120
(0.0, -0.09, 0.0)	(0.055, 0.055, 0.055)	(0, 0)	60
(0.0, -0.09, 0.0137)	(0.039, 0.039, 0.039)	(0, 0)	60
(0.0, -0.09, 0.0238)	(0.0234, 0.0234, 0.0234)	(0, 0)	60
(0.0, -0.09, 0.0316)	(0.0156, 0.0156, 0.0156)	(0, 0)	60
(0.0, 0.62, -0.25)	(0.022, 0.022, 0.022)	(0, 0)	30

* Last row of the table lists the parameters of the lesion used in the ROC and HT studies.

III. RESULTS

A modified three dimensional (3D) Shepp-Logan head phantom was used to demonstrate the proposed noise reduction scheme for low-dose HCT. Table I lists the parameters of ellipsoids (or objects) for the phantom of size 2×2×2 mm^3 and in this study the phantom was scaled uniformly to size of 256×256×256 mm^3 (i.e., the voxel side size is 1 mm). The phantom was oriented with its *z*-axis along the longitudinal axis of the scanner and the longitudinal width of the detector band was 1 mm. The pitch for the scanning was chosen as 1.5:1. The source-to-isocenter distance was 600 mm. For each 2π rotation, 512 fan-beam projections each of 512 bins or channels were simulated. At a rotating angle and axial position *z*, each projection datum along a ray through the phantom was computed based on the known densities and intersection lengths of the ray with the geometric shapes of the

objects in the phantom. After the sinogram was computed, a signal dependent Gaussian noise was added according to equation (1). The noisy sinogram was then processed by different noise filtering methods. Some preliminary results are shown in Figures 1, 2 and 3, where a standard FBP (with the Ramp filter at the Nyquist frequency cutoff) and conventional FBP (with the Hanning filter by an optimal cutoff frequency) are compared to the KL-PWLS noise filtering, followed by the standard FBP.

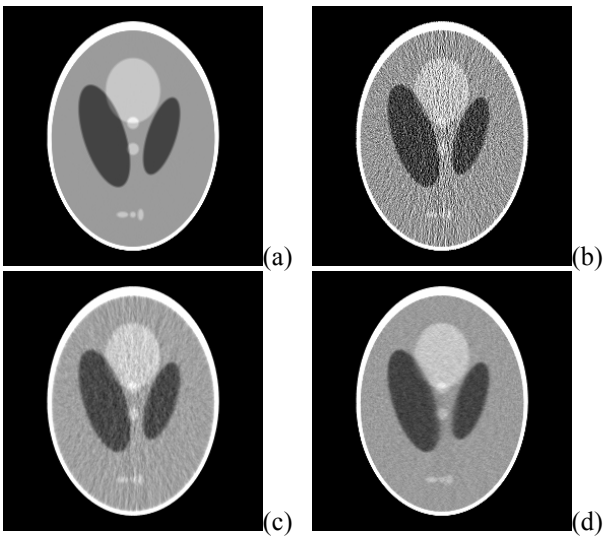

Figure 1: Transversal slice of the modified 3D Shepp-Logan phantom: (a) noise free image, (b) noisy image by FBP with the Ramp filter, (c) FBP image with the Hanning filter, and (d) FBP image from the KL-PWLS smoothed sinogram.

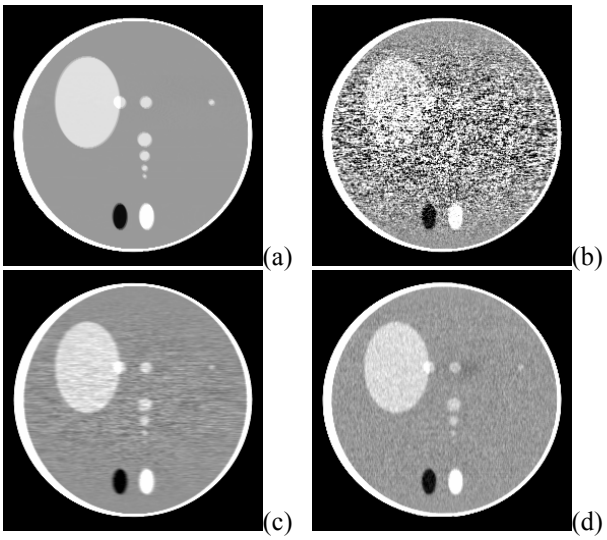

Figure 2: Sagittal slice of the modified 3D Shepp-Logan phantom: (a) noise free image, (b) noisy image by FBP with the Ramp filter, (c) FBP image with the Hanning filter, and (d) FBP image from the KL-PWLS smoothed sinogram.

Figure 1 shows a transversal slice of the phantom and the reconstructed images by different noise filtering methods. Figure 2 shows a sagittal slice of the phantom and the reconstructed images by different noise filtering methods. It can be observed that in the image reconstructed from the KL-PWLS smoothed sinogram, the noise is greatly suppressed while resolution is satisfactorily preserved. The observation is further confirmed by plotting the profiles along the *z*-axis of the phantom as shown in Figure 3. The comparison suggests that higher low-contrast detectability can be achieved by our KL-PWLS scheme as compared to the optimized Hanning filter. This expectation is realized below.

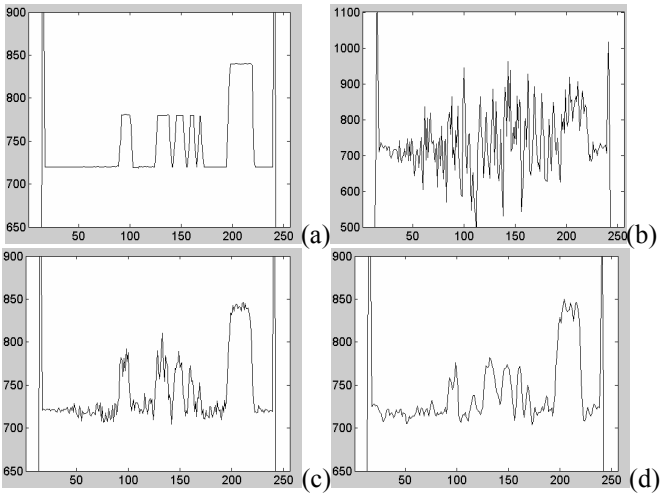

Figure 3: Vertical profiles through the center of the images in Figure 2.

To quantitatively evaluate the performance of the proposed KL-PWLS filtering scheme with comparison to the optimized Hanning filter, observer studies were performed using the ROC curve and the HT calculation.

A. ROC Study

One generally accepted method for evaluation of the performance of a medical imaging system or procedure is to evaluate the ability of an observer to detect an abnormality. By the observer study, a variety of pairs of true positive fraction (TPF) and false positive fraction (FPF) is generated as an observer changes the confidence threshold, and a ROC curve is then drawn or fitted from the obtained TPF and FPF [9]. Each ROC curve describes the inherent discrimination capacity of an imaging system or procedure. A common merit for comparing the ROC curves is the area under the curve (AUC) or A_Z. The filtering scheme which generates a larger AUC usually reflects a better detectability on abnormality.

To perform the ROC study, we carefully designed a low-contrast small lesion in the Shep-Logan phantom where the parameters of the lesion in the phantom are listed in the last row of Table I. Figure 4(a) shows a transversal slice of the phantom that contains the lesion volume, as indicated by an "arrow" in the picture. The noise-free sinograms of the phantom with and without the lesion were computed, respectively, using the same configuration and/or procedure as

described in Part III above. A total of 500 noisy sinograms were generated from each of the noise-free sinograms by adding signal-dependent Gaussian noise with variance determined by equation (1). Then these noisy sinograms were reconstructed by FBP with different noise filters: the optimized Hanning filter and the KL-PWLS strategy, resulting in a total of 2,000 images. A typical reconstructed image of the phantom with lesion by different noise filters, respectively, is shown in Figure 4.

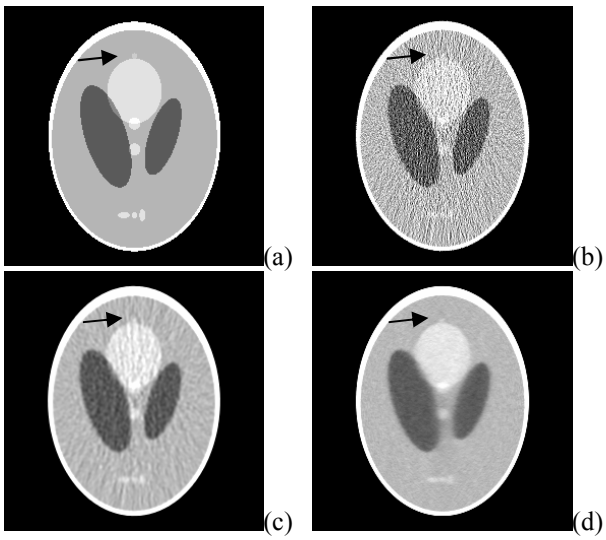

Figure 4: Transversal slice of the 3D Shep-Logan Phantom with a low-contrast small lesion: (a) noise free image, (b) noisy image by FBP with the Ramp filter, (c) FBP image with the Hanning filter, and (d) FBP image from the KL-PWLS smoothed sinogram. The arrow in each image indicate the location of the lesion.

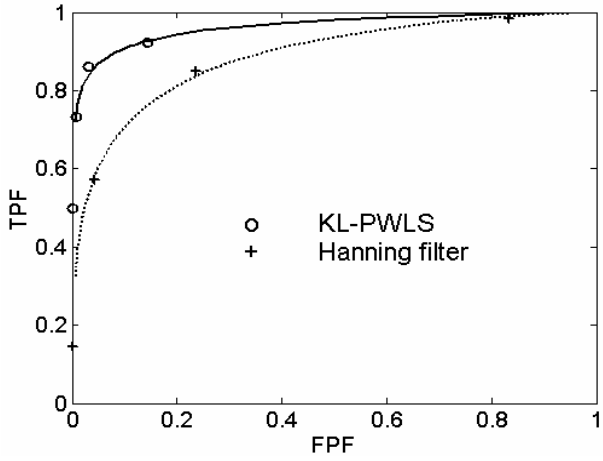

Figure 5: Results of ROC evaluation and the fitted ROC curves of the binormal model. The solid line and circles represent the KL-PWLS filtering scheme and the dashed line and cross marks stand for the Hanning filter result.

For each image, an observer was asked to select one of the five categories of confidence: (1) definitely or almost definitely negative, (2) probably negative, (3) possibly positive, (4) probably positive, and (5) definitely or almost definitely positive [9]. The scores were analyzed using the CLABROC code [10], resulted in four pairs of FPF and TPF for each filtering method, as plotted in Figure 5. The fitted ROC curves of the binormal model were also drawn in the figure. The area under the ROC curve for the KL-PWLS filtering scheme is 0.963 and the area under the ROC curve for the Hanning filter is 0.888. The one-tailed p-value is less than 0.005, which indicates that the difference between the two filtering schemes is statistically significant. These results indicate that the KL-PWLS strategy outperforms the Hanning filter in terms of detectability of abnormality in low contrast environment.

B. Hotelling Trace Calculation

Computer-based observers mimicking human observers have been proposed to alleviate the need for observers' interactions. One of these methods is the Hotelling observer for comparison of two imaging systems. In this method, the Hotelling trace [11], which is a measure of object class separability based on first and second-order statistics, is used to evaluate the ability of a system in separating between classes. In fact, Fiete *et al.* [12] found that the HT correlates with human performance in liver defect detection and Wollenweber *et al.* [13] recently implemented the HT to evaluate the potential increase in defect detection in myocardial SPECT (single photon emission computed tomography) using high-resolution fan-beam collimator versus parallel-hole collimation. Several other applications have also been reported recently. For example, Han *et al*. [14] employed the HT calculation to measure the gain by varying focal fan-beam collimation over parallel-hole geometry in quantitative chest SPECT. Li *et al*. [15] applied the HT calculation to measure the similarity of iterative and analytical reconstruction of quantitative brain SPECT considering Poisson noise, non-uniform attenuation (absorption and scatter) and point spread function (PSF) variation. All these computer-based observer studies concur with the human ROC results.

The mathematical formalism for calculating the HT is outlined below. For M classes of images, random samples are drawn to calculate the HT. Let $f_{j,m}$ be the j-th sample from class m, where $m = 1,2,\ldots, M$ and $j=1,2, \ldots, N_m$, and N_m be the number of samples from class M. Also suppose that the probability density function of occurrence for the sample $f_{j,m}$ is $p_{j,m}$. Define the inter-class scatter matrix S_1 and intra-class scatter matrix S_2 as follows:

$$S_1 = \sum_{m=1}^{M} p_m (\bar{f}_m - \bar{f})(\bar{f}_m - \bar{f})^T \tag{8}$$

$$S_2 = \sum_{m=1}^{M} p_m C_m \tag{9}$$

where

$$p_k = \sum_{j=1}^{N_m} p_{j,m} \tag{10}$$

is the *a priori* probability of occurrence of class k in all the samples;

$$\bar{f}_k = \sum_{j=1}^{N_k} \frac{p_{j,k}}{p_k} f_{j,k} \tag{11}$$

is the mean image of class k;

$$\bar{f} = \sum_{j=1}^{N_k} p_k \bar{f}_k \tag{12}$$

is the mean of mean class images which is also the grand mean of all images; and

$$C_k = \sum_{j=1}^{N_k} \frac{p_{j,k}}{p_k} (f_{j,k} - \bar{f}_k)(f_{j,k} - \bar{f}_k)^T \tag{13}$$

is the covariance matrix for the k-th class. With the above definitions, the HT is defined as:

$$J = tr\,(S_2^{-1} S_1)\,. \tag{14}$$

From the above definitions, the dimension of the scatter matrices is equal to the number of pixels (or voxels) in the image, which is huge. The main difficulty in calculating J value therefore lies in inverting the matrix S_2. Matrix S_2 is singular if the number of sample images is less than the number of voxels in the image. The requirement that the number of sample images be not less than the number of voxels in the image would consume too much disk storage or computer memory. Abbey *et al.* [16] suggested the use of subsets of the images, instead of the whole images, to reduce the amount of required space or data to calculate the J value.

The HT value J was then calculated using the above formalism with the images reconstructed in the previous section. The two classes of reconstructed images are those with and without the lesion respectively. In one study, the proposed KL-PWLS filtering scheme was used, and in the other study, the optimized Hanning filter was used. Different sizes of ROI containing the lesion were chosen for the calculation of the HT and the results are shown in Table II. As shown in the table, the HT J values given by the KL-PWLS filtering scheme are larger than the values given by the Hanning filter no matter what size of ROI were chosen. These results concur with the ROC measures and indicate that the performance of the KL-PWLS filtering scheme is superior to the Hanning filter in terms of low-contrast lesion detectability.

TABLE II
HOTELLING TRACE J FOR FBP RECONSTRUCTED IMAGES BY KL-PWLS AND HANNING FILTER

ROI (pixels x pixels)	15 x 15	20 x 20	25 x 25
KL-PWLS	6.32	8.97	15.9
Hanning	4.03	6.03	10.8

IV. CONCLUSION

In this study, we proposed a KL domain PWLS method to reduce noise in low-dose single-slice helical CT sinogram. The proposed method is based on the noise properties of low-dose CT sinogram. The KL transform is first applied along the neighboring projection slices and then the PWLS criterion is employed to estimate the noise-free projection data for each KL component. After inverse KL transform on the processed projection data, an interpolation is applied for full-scan data, followed by the FBP reconstruction to generate the low-dose CT images of the phantom. By visual judgment, the proposed KL-PWLS filtering scheme can suppress noise efficiently while structures are satisfactorily preserved. Quantitative evaluation by ROC study and HT calculation reveals that the proposed KL-PWLS filtering scheme outperforms the optimized conventional low-pass Hanning filter in terms of lesion detectbility in low-contrast environment.

V. REFERENCES

[1] K Jung, K. Lee, S. Kim, T. Kim, Y. Pyeun and J. Lee, "Low-dose, volumetric helical CT: image quality, radiation dose, and usefulness for evaluation of bronchiectasis", *Invest. Radiology*, vol. 35, pp. 577-563, 2000.

[2] J. Hsieh, "Nonstationary noise characteristics of the helical scan and its impact on image quality and artifacts", *Medical Physics*, vol. 24, pp.1375-1384, 1997.

[3] H. Lu, X. Li, and Z. Liang, "Analytical noise treatment for low-dose CT projection data by penalized weighted least-square smoothing in the K-L domain," *SPIE Medical Imaging*, vol. 4682, pp. 146-152, 2002.

[4] H. Lu, I. Hsiao, X. Li, and Z. Liang, "Noise properties of low-dose CT projections and noise treatment by scale transformations," *Conf. Record IEEE NSS-MIC*, in CD-ROM, 2001.

[5] T. Li, J. Wang, J. Wen, X. Li, H. Lu, J. Hsieh, and Z. Liang "SNR-weighted sinogram smoothing with improved noise-resolution properties for low-dose X-ray computed tomography" *SPIE Medical Imaging*, vol. 5370, pp. 2058-2066, 2004.

[6] T. Li, X. Li, J. Wang, J. Wen, H. Lu, J. Hsieh, and Z. Liang, "Nonlinear sinogram smoothing for low-dose X-ray CT," *IEEE Trans. Nuclear Science*, in press, 2004.

[7] M. N. Wernick, E. J. Infusino, and Milošević "Fast spatio-temporal image reconstruction for dynamic PET" *IEEE Trans. Medical Imaging*, vol. 18, pp.185-95, 1999.

[8] C. R. Crawford and K. F. King, "Computed tomography scanning with simultaneous patient translation", *Medical Physics*, vol. 17, pp. 967-981, 1990.

[9] C. E. Metz, "ROC methodology in radiological imaging", *Invest. Radiology*, vol. 21, pp. 720-733, 1986.

[10] C. E. Metz, P-L Wang, and H. B. Kroman, "A new approach for testing the significance of differences between ROC curves measured from correlated data", *Inform. Process. Med. Imaging*, pp. 432-445, 1984.

[11] H. Hotelling, "The generalization of student's ratio", *Annals. Math. Stat*. vol. 2, pp. 360-378, 1931.

[12] R. D. Fiete, H. H. Barrett, W. E. Smith, and K. J. Myers, "Hotelling trace criterion and its correlation with human-observer performance", *J Opt Soc Amer A*, vol. 4, pp. 945-953, 1987.

[13] S. D. Wollenweber, B. M. W. Tsui, D. S. Lalush, E. C. Frey, and G. T. Gullberg, "Evaluation of myocardial defect detection between parallel-hole and fan-beam SPECT using the Hotelling trace", *IEEE Trans. Nuclear Science,* vol. 45, pp. 2205-2210, 1998.

[14] G. Han, W. Zhu, and Z. Liang, "Gain of varying focal-length fan-beam collimator for cardiac SPECT by ROC, Hotelling trace, and bias-variance measures," *J. Nucl. Medicine*, vol. 42, pp. 7, 2001.

[15] T. Li, J. Wen, and Z. Liang , "Performance evaluation of analytical- and iterative-based quantitative brain SPECT reconstruction with fan-beam collimation by both Human (ROC) and computer (CHO) observers, as well as bias-variance plot", *J. Nucl. Medicine*, vol. 45, pp. 46, 2004.

[16] C. K. Abbey, H. H. Barrett, and M. P. Eckstein, "Practical issues and methodology in assessment of image quality using model observers", *SPIE Medical Imaging*, vol. 3032, pp. 182-194, 1997.